Terahertz Faraday rotation of $SrFe_{12}O_{19}$ hexaferrites enhanced by Nb-doping

Zimeng Hu[a], Gavin B.G. Stenning[b], Vladimir Koval[c], Jiyue Wu[a], Bin Yang[d], Alisa Leavesley[e,f],*

Richard Wylde[f], Michael John Reece[a], Chenglong Jia[g], and Haixue Yan[a*]*

[a] School of Engineering and Materials Science, Queen Mary University of London, Mile End Road, London E1 4NS, United Kingdom

[b] ISIS Neutron and Muon Source, Rutherford Appleton Laboratory, Didcot, Oxfordshire OX11 0QX, United Kingdom

[c] Institute of Materials Research, Slovak Academy of Sciences, Kosice 04001, Slovakia

[d] Faculty of Science and Engineering, University of Chester, Parkgate Road, Chester, CH1 4BJ, United Kingdom

[e] Virginia Diodes Inc., 979 2nd St SE #309, Charlottesville, VA 22902, USA

[f] Thomas Keating Ltd, Billingshurst, West Sussex RH14 9SH, United Kingdom

[g] Key Laboratory for Magnetism and Magnetic Materials of MOE, Lanzhou University, Lanzhou 730000, P. R. China

ABSTRACT

The magneto-optical and dielectric behaviour of M-type hexaferrites as permanent magnets in the THz band are essential for potential applications like microwave absorbers and antennas, while are rarely reported recent years. In this work, single-phase $SrFe_{12-x}Nb_xO_{19}$ hexaferrite ceramics were prepared by conventional solid state sintering method. Temperature-dependent of dielectric parameters were investigated here to search the relationship between dielectric response and magnetic phase transition. The saturated magnetization increases by nearly 12% while the coercive field decreases by 30% in the $x = 0.03$ composition compared to that of the $x = 0.00$ sample. Besides, Nb substitution improves the magneto-optical behaviour in the THz band by comparing the Faraday rotation parameter from 0.75 ($x = 0.00$) to 1.30 ($x = 0.03$). The changes in the magnetic properties are explained by a composition-driven increase of the net magnetic moment and enhanced ferromagnetic exchange coupling. The substitution of donor dopant Nb on the Fe site is a feasible way to obtain multifunctional M-type hexaferrites, as preferred candidates for permanent magnets, sensors and other electronic devices.

INTRODUCTION

Magnetic materials like hexaferrites [1, 2] and spinel ferrites [3, 4] have been investigated for decades due to their advanced electronic and magnetic performances and potential applications. M-type hexaferrites having the general formula $MeFe_{12}O_{19}$ (Me is a divalent ion like Ca, Sr, Ba, Pb, *etc.*) are widely studied for sensing and imaging applications as well as for advanced multi-state memory devices, transducers and RF/MW filters [5, 6]. Their unique magnetic, dielectric, and multiferroic properties originate from their large magneto-crystalline anisotropy along the *c*-axis and collective displacement of iron ions in the FeO_5 bipyramidal units. The crystal structure of M-type hexaferrites is hexagonal with the space group P6$_3$/mmc. The P6$_3$/mmc unit cell consists of RSR*S* layers, where S = $Fe_6O_8^{2+}$ is the spinel block and R = $MeFe_6O_{11}^{2-}$ is the hexagonal block. The R*S* layers are RS layers rotated around the *c*-axis by 180°. Fe^{3+} ions occupy five different sites showing opposite spin rotations: at the 12*k*, 2*b*, and 2*a* octahedral sites, the spins have the up ↑ direction and at the 4*f$_1$* and 4*f$_2$* sites, the spins are aligned in the down ↓ direction [7]. As a consequence, the M-type hexaferrites show ferrimagnetic behaviour at room temperature.

Among the M-type hexaferrites, $SrFe_{12}O_{19}$ has become one of the most studied hard ferrites due to its high coercive field (H_c = 5.55 kOe) [8], high Curie temperature (T_c = 460 °C) [9], large saturation magnetization (M_s = 0.056 emu/mg), and large remnant magnetization (M_r = 0.016 emu/mg) [2, 9]. $SrFe_{12}O_{19}$ can be prepared at low costs, which makes it an attractive material for commercial use. However, achieving larger saturated magnetization and, at the same time, appealing dielectric behaviour remains a big challenge in designing and preparing high-performance hexaferrites derived from $SrFe_{12}O_{19}$.

The most promising approach to synthesize the $SrFe_{12}O_{19}$-based hexaferrites and tailor their functional properties for desired applications is a partial substitution of Sr^{2+} ions by isovalent Ba^{2+},

Pb^{2+} and Ca^{2+} ions [10-13] or trivalent rare earths [14] like La^{3+}, Nd^{3+} and Sm^{3+}. Doping at Sr sites by La^{3+} ion with smaller radii has been reported to decrease both saturated and remnant magnetization of $SrFe_{12}O_{19}$ [14, 15]. It was shown that the La^{3+} substitution makes the valence variation from Fe^{3+} to Fe^{2+} and non-collinear spin arrangement of magnetic moments, which results in this decrement of magnetization [14]. In addition, substitution with rare earths can significantly increases the grain size of $SrFe_{12}O_{19}$-based ceramics, further enlarging the magnetic coercive field [14].

Another strategy to improve the functional properties of the M-type hexaferrites is a partial substitution of the Fe ions by dopants: (i): isovalent ions such as Sc^{3+} [16], Ga^{3+} [17], Al^{3+} [18, 19] and In^{3+} [20]; (ii): Co^{2+} ions [21, 22] or Nb^{3+} [23]; (iii): ionic combinations like Cr^{3+}-Zn^{2+} [24], Co^{4+}-Ca^{2+} [21] or Zr^{4+}-Cd^{2+} [7]. For example, the coexistence of electrical and magnetic ordering at room temperature was observed in modified $SrFe_{12-x}In_xO_{19}$ magnetoelectric multiferroic ceramics [25, 26]. The co-introduction of Co^{4+} and Ca^{2+} ions on Fe sites in $BaFe_{12}O_{19}$ can increase the dielectric permittivity, if compared to the undoped one, due to a higher concentration of Fe^{3+} ions in the high spin state [21]. The reduced grain size, increased saturated magnetization and large magneto-crystalline anisotropy were obtained in the Nb-substituted $BaFe_{12}O_{19}$ [23]. In addition, the introduction of Nb^{3+} ions can help to decrease both the alternating current (AC) conductivity and direct current (DC) conductivity of the M-type hexaferrites, which suggests the potential function of Nb for improving dielectric behaviour [27]. Asghar and Anis-ur-Rehman have proposed, based on the Maxwell-Wagner two-layer theory, that the highly resistive grain boundaries are responsible for reduced conductivity of hexaferrites in the dielectric measurements [24, 28]. Above mentioned AC studies, however, were carried out on M type hexaferrites within a narrow frequency range. To date, only a few reports on the dielectric behaviour of M-type hexaferrites at terahertz (THz) frequencies [29, 30], much less study on Faraday rotation [31], knowledge of which is crucial for construction of

optical-communication devices. Moreover, a comprehensive study on the dielectric properties of hexaferrites over a wide frequency and temperature range is missing. Also, for future perspectives, it is also necessary to search for new hexaferrites with tunable dielectric, magnetic, and even magnetodielectric properties.

As the Nb^{5+} ion can electrically compensate the presence of the Fe^{2+} ions and simultaneously inhibit abnormal grain growth in polycrystalline $SrFe_{12}O_{19}$, a study on the dielectric and magnetic properties of the $SrFe_{12}O_{19}$ ceramics (with and without Nb doping) was undertaken in order to explore the relationship between the composition, structure and functional properties of these hard ferrites. Here, two compositions of the $SrFe_{12-x}Nb_xO_{19}$ (x = 0.00 and 0.03) were designed. Additionally, for the first time, a modified technique of THz spectroscopy is introduced in order to study the Faraday rotation effect in hexaferrites. Finally, using this technique we demonstrate that the Nb-doped $SrFe_{12}O_{19}$ ceramics possess large relative permittivity and Faraday rotation at THz frequencies, suggesting the Nb modified M-type hexaferrites useful in optical communication devices, security surveillance systems, and sensing applications.

MATERIALS AND METHODS

Materials

Hexaferrite ceramics can be prepared by solid-state sintering method [22], sol-gel method and green pulsed laser ablation in liquid (PLAL) approaches [32, 33]. Here, $SrFe_{12-x}Nb_xO_{19}$ ceramics, with x = 0.00 and 0.03 (abbreviated as SFO and SFN3O), were prepared by the conventional solid-state method using raw materials of $SrCO_3$ (purity $\geq$ 99.9%, Aldrich), Nb_2O_5 (purity $\geq$ 99.9%, Alfa Aesar), and Fe_2O_3 (purity $\geq$ 99.945%, Alfa Aesar). The chemicals were pre-heated at 200 °C for 24 h and then weighed according to the stoichiometric formula. They were ball milled in ethanol

5

for 12 h at 250 rpm using stainless balls and vessels. The slurry was dried, and the powder product was calcined at 1100 °C for 6 h. To reduce particle size, the calcined powder was ball milled again. The fine precursor was mixed with 5wt % PVA and then pressed into pellets with a diameter of 13 mm and thickness of 1-2 mm. The pellets were heated at 800 °C for 2 h in air to remove the binder. Sintering was carried out at 1200 °C for 6 h in air. The sintered pellets were polished, and then annealed in air for 12 h at 1000 °C.

Methods

The crystal structure of the sintered ceramics was investigated by X-ray powder diffraction (XRD, PANalytical, Cubix) on crushed powders using Ni-filtered Cu Kα radiation ($\lambda = 1.5418$ Å) over the 2θ range from 5 to 120° with a step of 0.0315°. Structural analysis was performed using Rietveld refinement using the EXPGUI and GSAS software packages [34, 35]. The surface morphology of the polished and thermally etched samples was observed by scanning electron microscopy (SEM). The surface element analysis was performed with an X-ray photoelectron spectrometer (XPS, Nexsa). Thermal analysis was carried out by differential scanning calorimetry (DSC, Rheometric Scientific, a model STA 1500 H) in N_2 from 25 °C to 800 °C with a heating/cooling rate of 10 °C/min. For the dielectric measurements, the as-sintered samples were ground to less than 0.5 mm thickness and then coated with silver paint (Gwent Electronic Materials Ltd., C2011004D5, Pontypool, UK). The temperature dependence of the relative dielectric permittivity (ε') and loss tangent (tan δ) were measured in the temperature range 25 °C - 600 °C at three different frequencies (100 kHz, 500 kHz and 1 MHz) via a computer-controlled system with an LCR meter (Agilent, 4284A, USA) attached to a furnace. The field dependent magnetization ($M - H$) loops of the samples at room temperature, and the zero-field cooling (ZFC) and field

cooling (FC) magnetizations were measured over the temperature range 1.8 K – 400 K at 1000 Oe using a superconducting quantum interference device (SQUID, Quantum Design, USA). The dielectric properties and Faraday rotation in the THz region were measured by modified Terahertz Time-domain Spectroscopy (THz-TDS, TeTechs Ltd., Canada) in transmission mode. Electromagnetic radiation ranging from 0.2 THz to 0.8 THz was used to illuminate tiny wafers with a thickness of 1 mm and a diameter of 12 mm. The collected THz time-domain spectra were Fourier transformed to obtain both amplitude and phase information in the frequency domain. All information in the frequency domain was used to extract the permittivity and loss tangent data of the samples [31, 36]. The permittivity and loss tangent in the THz band were converted from the refractive index of virgin samples. After magnetizing at a magnetic field of 3500 Oe, the samples were tested in the THz band with right-handed and left-handed gratings to study the Faraday rotation effect.

RESULTS AND DISCUSSION

A schematic of the crystal structure of $SrFe_{12}O_{19}$ hexaferrite is illustrated in Fig. 1a. Fig. 1b shows the room-temperature XRD patterns of the $SrFe_{12-x}Nb_xO_{19}$ ($x = 0.00, 0.03$) ceramics. Both SFO and SFN3O are single-phase materials with a hexagonal structure (space group: $P6_3/mmc$). The Miller indices are labelled based on the reference $SrFe_{12}O_{19}$ standard (ICSD no. 69022), and are in good agreement with Kimura's work on the structural analysis of $SrFe_{12}O_{19}$ [18]. The Nb^{5+} ions can enter both the octahedral and tetrahedral sites based on previous work [23, 37]. Here, Nb^{5+} ions prefer occupying the spin down $4f_1$ and $4f_2$ sites. The fitted well XRD patterns within selected range 20-120° for SFO and SFN3O are shown in Fig. S1a and S1b, respectively. The χ^2 factor for good fitting does not exceed 2.7. The refinement and crystal parameters are listed in Table S1. In

diffractograms, no secondary phase is observed within the detection limit of the X-ray diffractometer. Thus, the substitutional niobium ions are supposed to incorporate in the lattice. Because of the smaller ionic radius of Nb^{5+} (0.640 Å) compared to that of Fe^{3+} (0.645 Å) [38], the volume of the unit cell decreases on doping from 692.887(2) ($Å^3$) to 692.262(3) ($Å^3$), and thus the shifting of diffraction peaks towards higher angles is observed for SFN3O in Fig.1b inset, indicated by blue short-dotted lines. The etched microstructures of the SFO and SFN3O ceramics are shown in Figs. 1c and 1d, respectively. As can be seen, the grains are closely packed in both samples. This observation is consistent with the high relative density of the ceramics (> 95%) measured using the Archimedes method. It should be noticed that the grain size decreases with Nb doping from 1.85 µm (SFO) to 1.43 µm (SFN3O), which is in accordance with SEM observations of other Nb-doped dielectric ceramics [39]. It should be noted that decreasing grain size results in a smaller unit cell volume due to larger surface tension forces, as reported in other magnets [40, 41].
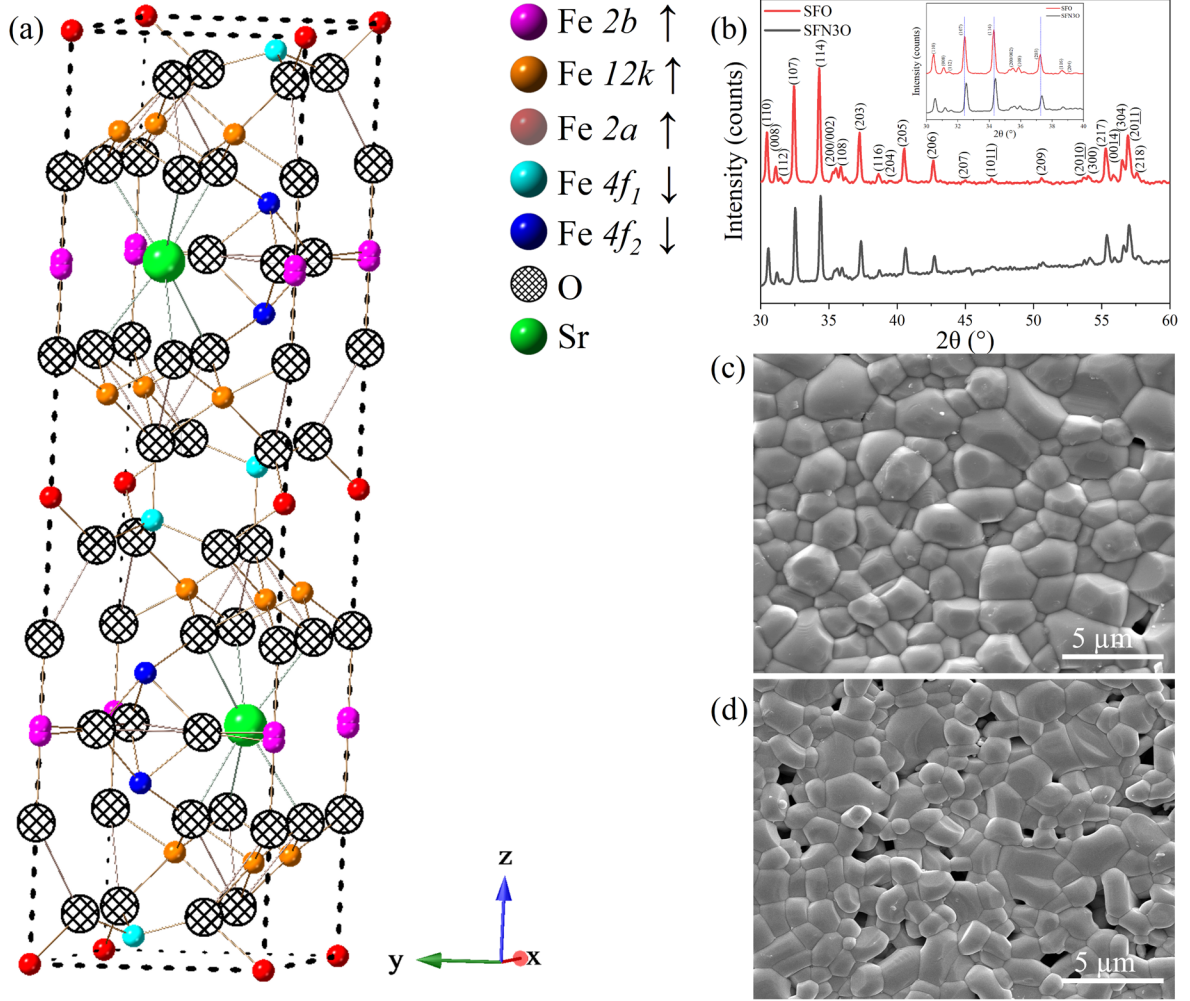
Figure 1. (a): A schematic of the crystal structure of pure $SrFe_{12}O_{19}$ hexaferrite. (b): XRD patterns of $SrFe_{12-x}Nb_xO_{19}$ (x = 0.00, 0.03) ceramics within the selected 30-60° range, indexing was performed based on the reference standard $SrFe_{12}O_{19}$ (ICSD no. 69022). Inset: Enlarged view of XRD patterns within 30-40°. (c) and (d) SEM images of the thermally etched ceramics with x = 0.00 and 0.03 ceramics, respectively.

The dielectric and magnetic properties of hexaferrites strongly depend on the content of Fe ions and oxygen vacancies [29]. Therefore, information on the oxidation state of Fe, which is closely related to oxygen vacancies and changes due to processing at high temperatures, is of a great

importance. To explore the effect of the Nb substitution on the valence of Fe in the prepared hexaferrites, X-ray photoelectron spectroscopy was employed. The fitted O1s XPS spectra of SFO and SFN3O are shown in Figs. 2a and 2b, respectively. The spectra were fitted by the Avantage software using the Gaussian-Lorentzian product (GLP) [42]. The results of fittings are summarized in Table S2. Apparently, the experimental O1s spectrum is formed by three spectral peaks - the red curve peak corresponds to the lattice oxygen (O_{latt}), the blue peak represents oxygen in a deficient environment (O_{vac}), and the green curve peak can be ascribed to chemisorbed or dissociated oxygen (O_{abs}) from the air [43, 44]. The ratio of integrated areas of O_{vac}:O_{latt} can be used to compare the change in relative oxygen vacancy concentration between compositions [45]. The binding energies of the O_{latt}, O_{vac} and O_{abs} peaks in SFO are 529.40 eV, 530.82 eV, and 532.78 eV, respectively. In SFN3O, the respective peaks are shifted to 529.56 eV, 530.86 eV and 532.99 eV. The reduced ratio O_{vac}:O_{latt} varies from 0.354(3) (SFO) to 0.222(1) (SFN3O), as calculated from the integral area of the corresponding peaks. Therefore, one can conclude that the concentration of oxygen vacancies decreases with Nb doping [46]. The reduced oxygen vacancies are expected to improve the dielectric properties of the Nb-doped hexaferrites [29].
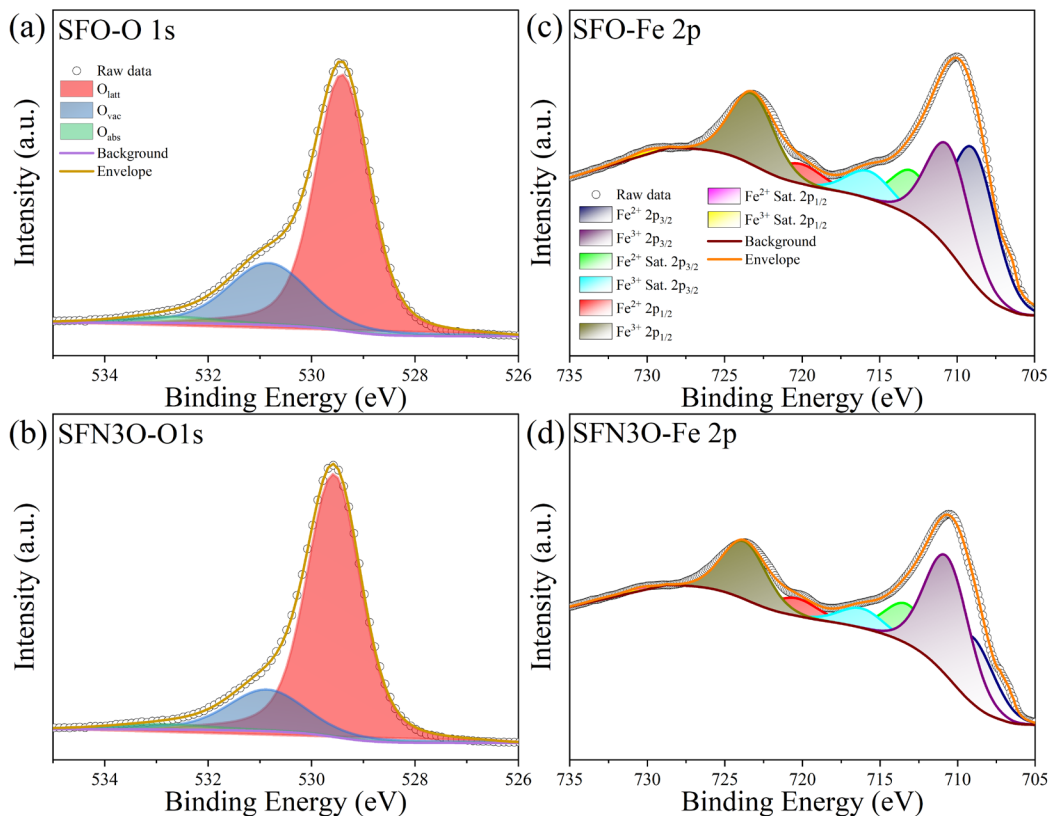
Figure 2. (a), (b): Fitted O 1s XPS spectra and (c), (d): Fitted Fe 2p XPS spectra for the SFO and SFN3O hexaferrites, respectively.

To further investigate the origin of oxygen vacancies, the valence of Fe ions was analyzed by fitting the Fe 2p spectra, as shown in Figs. 2c and 2d. The fitted results are listed in Table S3. The Fe 2p spectrum is formed by a typical doublet of Fe $2p_{3/2}$ and Fe $2p_{1/2}$ with satellite peaks corresponding to different valences of Fe [29, 47, 48]. A deconvolution of the characteristic Fe $2p_{3/2}$ photon emission peak in SFO yields a doublet with the Fe^{3+} $2p_{3/2}$ (~710.88 eV) and Fe^{2+} $2p_{3/2}$ (~709.18 eV) peaks, and in SFN3O the doublet is composed of the Fe^{3+} $2p_{3/2}$ (~711.08 eV) and Fe^{2+} $2p_{3/2}$ (~709.38 eV) peaks (depicted by the purple and blue curves in Figs. 2c and 2d). From the fitted spectra, a fraction of the Fe ions in the two chemical states was determined by the integrated area ratio. It was found that the area ratio of Fe^{2+} $2p_{3/2}$: Fe^{3+} $2p_{3/2}$ decreases from

11

1.076(8) in SFO to 0.592(3) in SFN3O, which indicates that the reduction of Fe^{3+} is suppressed by the Nb^{5+} doping. The increased oxidation degree of Fe ions reflected by XPS data is consistent with decreased oxygen deficiency discussed before, which also agrees well with previous work [49]. In addition, the decreased oxygen deficiencies agree well with smaller unit cell volume for SFO.

A phase evolution analysis of the SFO and SFN3O hexaferrites was performed by using the DSC thermograms, as recorded on heating and cooling (Fig. S2). Three thermal events, denoted as *a*, *b* and *c* are observed on the DSC curves for both samples. The first event *a* occurring at around 100 °C (on heating) indicates volatilization of the absorbed water [50]. The other two events *b* and *c* can be linked with magnetic phase transitions. For SFO, the thermal feature *b* is around 290 °C and *c* is around 465 °C; the latter agrees well with the reported ferromagnetic to paramagnetic phase transition temperature (the Curie temperature, T_c) of pure $SrFe_{12}O_{19}$ hexaferrite, 470 °C [9, 51]. Underlying mechanism of the *b* event needs a further investigation. Similar thermal events were observed for SFN3O, the event *b* at about 260 °C and *c* occurs at around 490 °C.

To further study the phase transition behaviour, the temperature dependencies of the relative dielectric permittivity (ε') and loss tangent (tan δ) of the SFO and SFN3O ceramics were measured in the temperature range 25 °C – 600 °C at three different frequencies, namely 100 kHz, 500 kHz and 1 MHz (Figs. 3a and 3d). At the Curie temperature, the arrangement of spins in ferrites changes from the long-range ordered ferromagnetic state to paramagnetic state with random orientations. The magnetic transitions are usually accompanied not only by changes of the magnetic properties but also variations in other physical properties, such as dielectric permittivity, specific heat, and so on [52]. For SFO, two broad dielectric anomalies with a strong frequency dependence are observed in ε'(T) in the regions I and II (Fig. 3a). It should be noted that the dielectric permittivity reflects the ability of electric dipoles to oscillate in an applied AC field [53]. Hence, the large decrease of the

permittivity with increasing frequency from 100 kHz to 1 MHz can be explained by a lower contribution of interfacial polarization or point defects to the permittivity at higher frequencies. The second dielectric anomaly over the regions II and III corresponds to the thermal feature *b* in Fig. S2 and indicates a magnetic phase transition. The maximum of the permittivity occurs at a characteristic temperature, which shifts towards higher temperatures with increasing frequency. The frequency dispersion and diffusion of both dielectric peaks (in region I and through the regions II and III) suggest that relaxation in the SFO hexaferrite can be attributed to point defects. The relaxation behaviour should obey the Arrhenius law in [54, 55] as shown in Figs. 3b and 3c:

$$\tau = \tau_0 \exp(-\frac{E_a}{k_B T}) \qquad (1)$$

where τ is the relaxation time of defects, τ_0 is a time constant, E_a is the activation energy, k_B is the Boltzmann constant, T is the temperature linked with the maximum of ε'. The fitted activation energy E_a (0.037 eV) and relaxation time τ_0 (3.8×10^{-8} s) for the first anomaly of SFO at around 100 °C suggest that the dielectric peak in region I is due to point defects, such as oxygen vacancies with long relaxation time. The second dielectric anomaly in the overlapping regions II and III is characterized by the values of $E_a = 0.283$ eV and $\tau_0 = 2.24 \times 10^{-11}$ s, which are characteristic of oxygen vacancies.

For the SFN3O sample, four dielectric anomalies with different dependence on frequency are observed at temperatures between 25 °C and 600 °C. In contrast to SFO, there is no anomaly in region I. With increasing temperature above 100 °C, a nearly frequency-independent permittivity anomaly occurs at around 270 °C in region II (Fig. 3d). The corresponding loss peak is presented in Fig. 3e. The fitted relaxation time $\tau_0 = 1.30 \times 10^{-9}$ s (see Fig. 3f for the Arrhenius law fitting) is similar to that obtained for SFO, suggesting a contribution to the dielectric permittivity from defects. Instead, the dielectric anomaly of the SFN3O ceramic at 270 °C can be linked with a

magnetic phase transition, which is consistent with the results of the DSC analysis (the event *b* in Fig. S2b). The third, most intense anomaly is a frequency independent feature occurring at about 400 °C. It is assumed that the loss peak at a slightly lower temperature (~370 °C) is caused by enhanced domain wall activity, typical of ferroelectric materials [53, 56]. It should be mentioned that the fourth dielectric anomaly at around 500 °C shows a diffuse behaviour but without a temperature shift. Moreover, this temperature is close to the thermal event *c* in the DSC curve (Fig. S2b), suggesting the ferrimagnetic-to-paramagnetic phase transition. It is obvious that the Nb substitution increases the Curie temperature of the $SrFe_{12}O_{19}$ hexaferrite, which agrees well with the earlier study of Wang *et al.* [57]. This finding is further supported also by the loss tangent minimum observed close to 500 °C [56]. The origin of the dielectric anomalies (either the phase transition or point defects) are still under debate. Further studies are necessary to clarify the anomalous high temperature critical behaviour of hexaferrites.
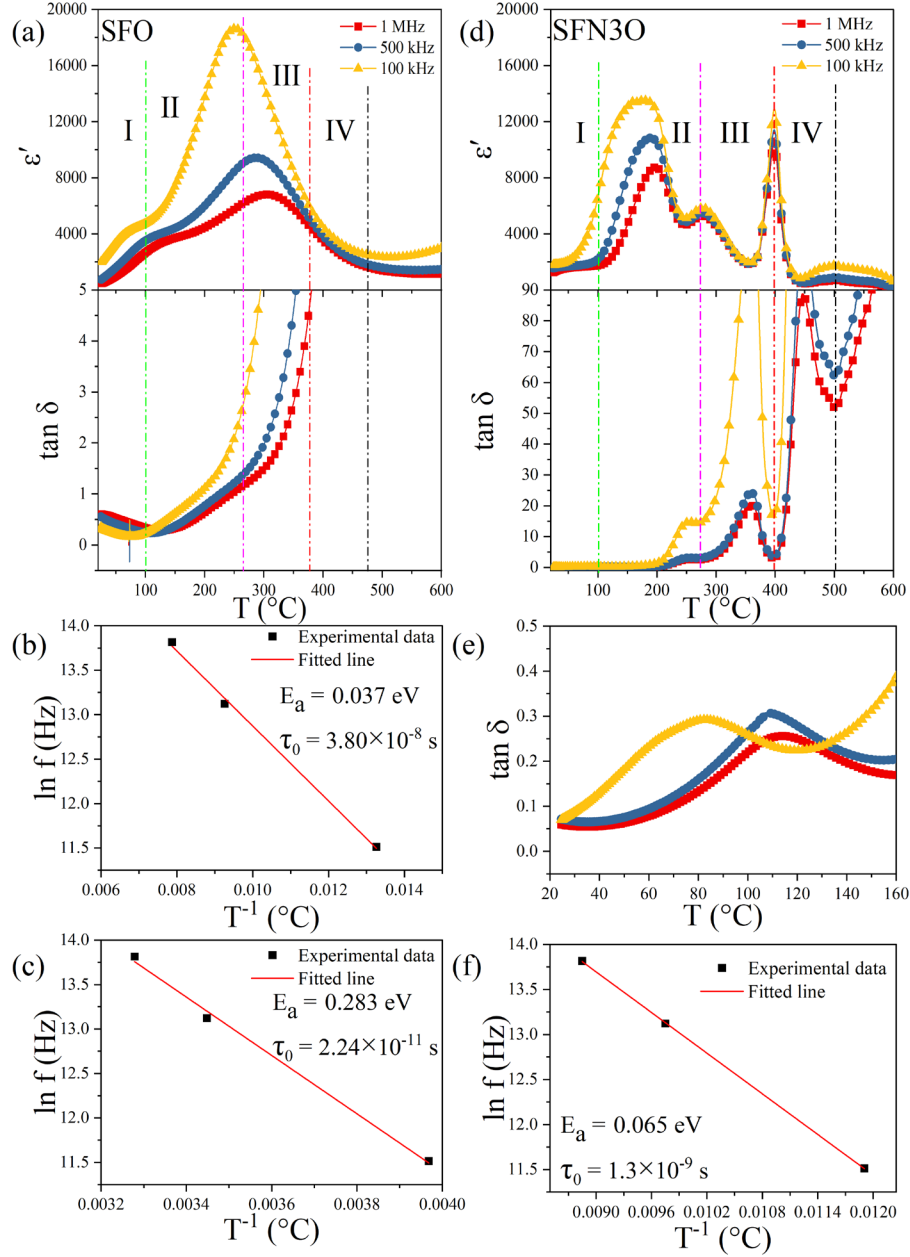
Figure 3. Temperature dependencies of the relative dielectric permittivity (ε') and loss tangent (tan δ) of SFO (a), and SFN3O (d). (b) and (c) Arrhenius law fittings of the dielectric peaks of SFO in region I and II, respectively. (e) The enlarged view of the loss tangent of SFN3O with a strong frequency dependence at temperatures between 25 °C and 160 °C. (f) the Arrhenius law fitting of the dielectric peak in the region II for SFN3O hexaferrite.

The FC (field cooling) magnetization and ZFC (zero-field cooling) magnetization as a function of temperature for the respective SFO and SFN3O samples are shown in Figs. 4a and 4b. At cryogenic temperatures, the FC magnetization increases from 0.013 emu/mg for SFO to 0.022 emu/mg for SFN3O. This increment of magnetization corresponds to the higher saturated magnetization M_s of SFN3O (see Table 1), as obtained from the $M - H$ hysteresis loops in Fig. 4c. For SFO and SFN3O, both the ZFC and FC magnetizations increase monotonously upon cooling from 300 K down to 100 K. Below 100 K, a plateau-like hump is observed due to the super spin-glass (SSG) behaviour [58]. Humbe *et al.* [59] have reported on the magnetization peak in hexaferrites occurring at the blocking temperature (T_b), where a magnetic structure changes from a superparamagnetic to ferrimagnetic one. No other peak corresponding to a possible phase transition from ferrimagnetic to paramagnetic phase is observed in Figs. 4a and 4b for the respective SFO and SFN3O ceramics over a temperature range of 1.8 - 400 K. Therefore, one can postulate that the two hexaferrites are ferrimagnets at room temperature.

Fig. 4c displays the *M-H* loops of the SFO and SFN3O samples measured at room temperature. Both SFO and SFN3O show a typical ferrimagnetic behaviour. The saturated magnetization M_s for SFO and SFN3O is 0.068 emu/mg and 0.076 emu/mg, respectively. Both M_s and M_r for SFO are higher than previous work [9] possibly due to different preparation methods but agree well with other published work [15]. According to earlier studies on the SFO-derived hexaferrites [60], a high value of M_s can be ascribed to the high concentration of Fe^{3+} ions in high spin state and enhanced ferromagnetic exchange interactions between Fe ions caused by decreased oxygen deficiencies [58]. In this case, non-magnetic Nb^{5+} ions replacing the Fe ions at *4f₁* and *4f₂* sites (spin down states) give rise to the increased net magnetic moment together due to the enhanced ferromagnetic exchange coupling along the *z*-axis via Fe^{3+}-O- Nb^{5+} bonds. This is consistent with fitted XRD

results and agrees well with previous findings that Nb or other diamagnetic ions prefer to enter the octahedral and tetrahedral sites of Fe in hexaferrites [23, 61-63] and the intensity of antiferromagnetic exchange interactions is weakened as oxygen vacancy decreases [64, 65].
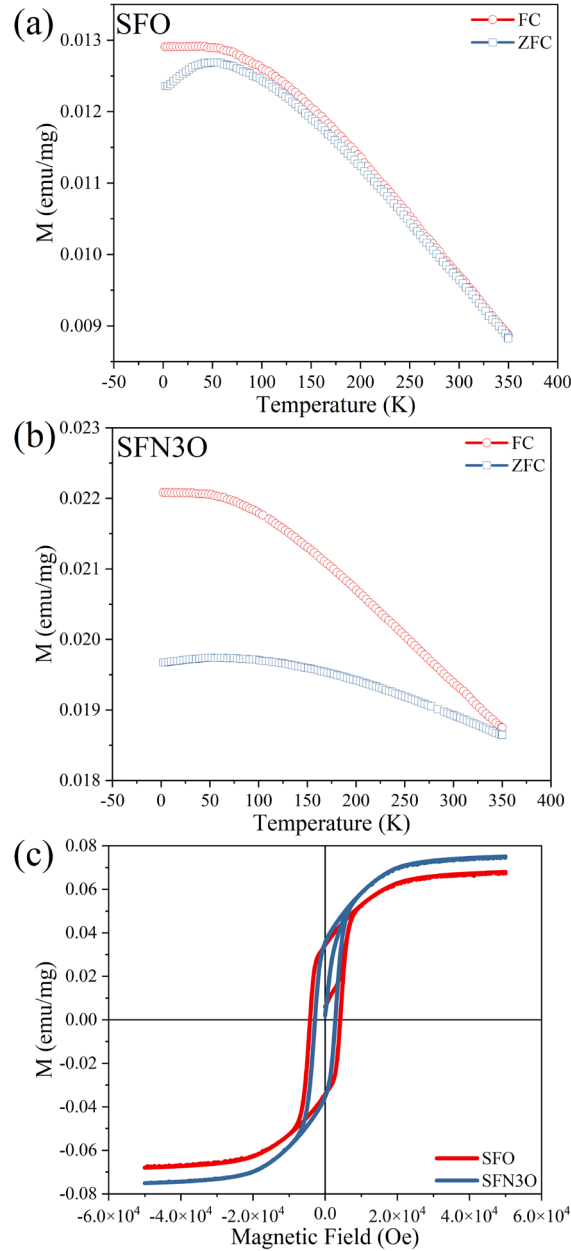

Figure 4. (a) and (b): The ZFC and FC magnetization curves for SFO and SFN3O, respectively. (c) The *M-H* hysteresis loops for SFO and SFN3O measured at 300 K.

It is expected that both SFO and SFN3O possess multi-domain structures with the squareness ratio ($M_{rs} = M_r/M_s$) 0.485 and 0.447, respectively [61, 66]. A slimmer M-H loop of SFN3O is observed in Fig. 4c, compared with SFO. According to the domain wall theory [67], $H_c \propto \frac{\sqrt{AH_A}}{M_s D}$, where A is the exchange stiffness, H_A is the magneto-crystalline anisotropy, M_s is the saturation magnetization and D is the grain size [68]. The coercive field H_c is proportional to the inverse M_s and smaller grain size [69, 70]. Therefore, one would expect that the dominant reason for a large drop in H_c nearly by 30% of SFN3O against the initial coercive field of SFO is the increment of saturation magnetization. The room-temperature magnetic parameters of the SFO and SFN3O samples are summarized in Table 1.

Table 1. Magnetic parameters of the SFO and SFN3O hexaferrites, as obtained at room temperature.

Composition	Saturated magnetisation M_s (emu/mg)	Remnant magnetisation M_r (emu/mg)	Coercive field H_c (Oe)	Squareness ratio M_{rs}
SFO	0.068	0.033	4200	0.485
SFN3O	0.076	0.034	2850	0.447

A schematic of the set-up for measurement of the THz transmission response is shown in Fig 5. Using this set-up, the Faraday rotation was determined by the refractive index measured for the left- and right-handed direction after magnetizing of the samples at a DC field of 3500 Oe. The permittivity was obtained from the measured refractive index n using the following equation:

$$n=\sqrt{\mu'\varepsilon'} \tag{2}$$

where μ', ε' is the relative permeability and relative permittivity, respectively. Fig. 6a shows the frequency dependencies of the dielectric permittivity and loss tangent of the as-prepared (non-magnetized) SFO and SFN3O samples in the THz band. The permittivity of both hexaferrites is nearly independent of the frequency due to a large ionic polarization and partly because of electronic polarization [71] within the 0.2-0.8 THz range. A slightly higher value of ε' and tan δ of SFN3O can be attributed to the smaller grain size effect, reduced coercive field and higher concentration of the ferrimagnetic active regions at THz frequencies. Figs. 6b and 6c show the respective complex refractive index for the right- and left-handed directions in the 0.2 - 0.8 THz range, n' is the real part while n'' is the imaginary part of refractive index. The value of $\Delta n'$ ($n'_{left-handed} - n'_{right-handed}$) is 0.75 for SFO and it greatly increases to 1.30 for SFN3O. This result clearly demonstrates that the Nb substitution improves the magnetic properties of pure SFO hexaferrite. Thus, the enhanced magneto-optical behaviour, namely the Faraday rotation effect in SFN3O can be attributed to the higher M_s and lower E_c. Moreover, the imaginary part of the right-handed refractive index (n'') of SFN3O shows a steeper decline with decreasing frequency than that of SFO, reaching a value of n'' of about 0.01 within 0.5 THz. This behaviour can be explained by the reduced oxygen vacancies and partial oxidation of Fe^{2+} ($Fe^{2+} \rightarrow Fe^{3+}$) during thermal treatment [29].
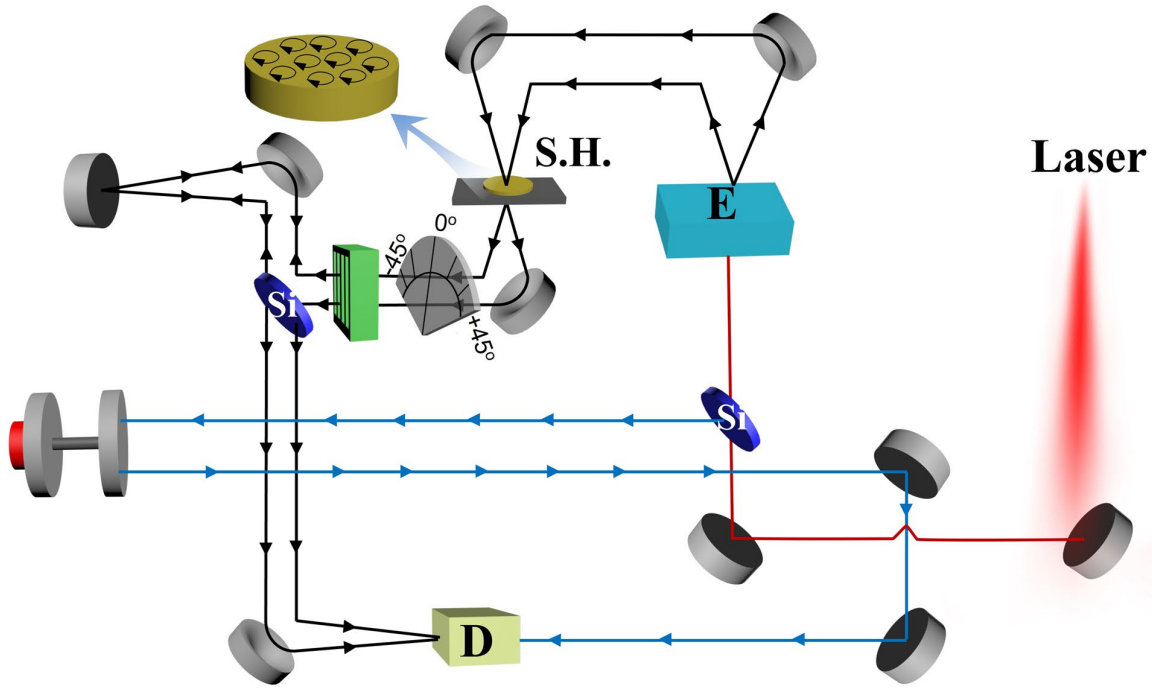
Figure 5. A schematic of the Faraday rotation measurement set up, based on the modified THz time-domain spectroscopy. M1-M5: flat reflection mirrors; Si: silicon wafer; E: THz photoconductive emitter; GPM1-GPM5: parabolic mirrors to focus and collimate THz beams; S.H: sample holder; D: THz photoconductive detector; AM: adjustable retroreflection mirror. The black lines guided by arrows are transmission THz beam and blue lines guided by arrows are 780 nm probe beam.

It can be concluded that the introduction of Nb into M-type hexaferrites is an effective way to improve their room-temperature ferrimagnetic properties and at the same time to enhance their dielectric behaviour in the THz band. The proposed chemical design with donor Nb^{5+} doping in the hexaferrites enables the development of advanced functional materials with improved magneto-optical properties and low dissipation for high-performance imaging and sensing applications in the THz band.
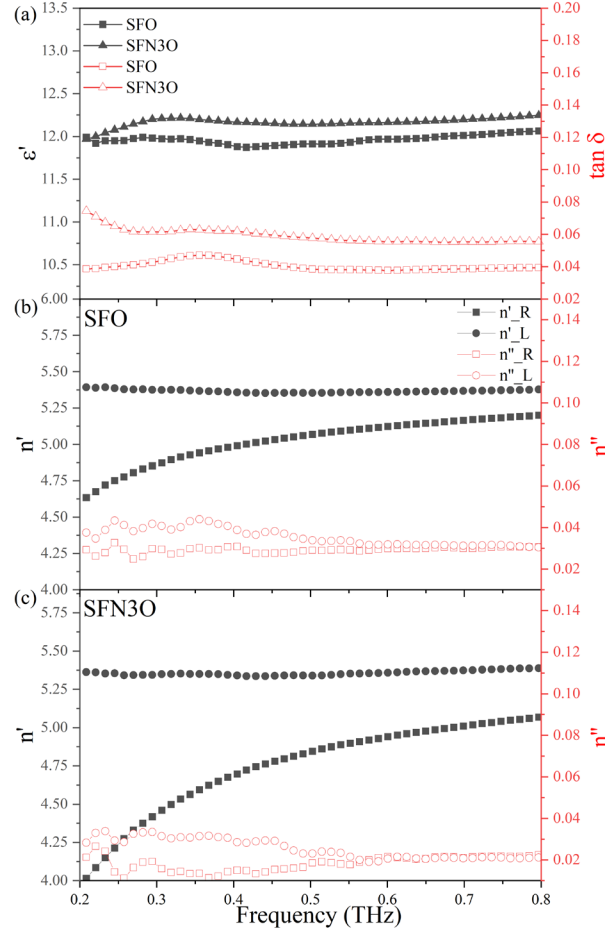
Figure 6. (a) The relative dielectric permittivity and loss tangent of the as-prepared SFO and SFN3O samples at the 0.2-0.8 THz band. (b) and (c): The complex refractive index of right- and left-handed directions for the magnetized SFO and SFN3O samples, respectively, at frequencies from 0.2 THz to 0.8 THz.

CONCLUSIONS

The M-type hexaferrites of $SrFe_{12-x}Nb_xO_{19}$ ($x = 0.00$ and 0.03) were prepared by solid-state reaction. The room-temperature XRD data demonstrate that the two ceramics are single-phase materials with the $P6_3/mmc$ space group. The mixed valence states of Fe (Fe^{3+}/Fe^{2+}) together with oxygen vacancies were revealed by XPS analysis, with SFN3O having fewer oxygen vacancies

than SFO. SQUID measurements of the field dependence of magnetization and ZFC/FC magnetization over the temperature range 1.8 – 400 K evidenced the ferrimagnetic behaviour of these two compositions. The increased saturated magnetization (0.076 emu/mg) in the $x = 0.03$ sample was explained by the preferred arrangement of Fe^{3+} ions in the spin up state. The composition driven enhancement of both multi-domain structure and ferromagnetic exchange coupling led to a higher saturation and lower coercivity of the Nb-doped hexaferrite. Moreover, this enhanced magnetic performance is accompanied by large Faraday rotation ($\Delta n' = 1.30$) and high relative permittivity in the THz band. Overall, the Nb-doped $SrFe_{12}O_{19}$ hexaferrite with the excellent magnetic properties in the THz band provides a competitive performance for microwave devices, filters and recording media.

ASSOCIATED CONTENT

Supporting Information

The following files are available free of charge.

Fitted XRD patterns at room temperature, crystal and refinement parameters, fitted results for O 1s and Fe 2p XPS spectra and DSC thermograms in heating and cooling regimes for SFO and SFN3O, (PDF).

AUTHOR INFORMATION

Corresponding Authors

*Bin Yang - Faculty of Science and Engineering, University of Chester, Parkgate Road, Chester, CH1 4BJ, United Kingdom; Email: b.yang@chester.ac.uk

*Chenglong Jia- Key Laboratory for Magnetism and Magnetic Materials of MOE, Lanzhou University, Lanzhou, 730000, P. R. China; Email: cljia@lzu.edu.cn

*Haixue Yan - School of Engineering and Materials Science, Queen Mary University of London, Mile End Road, London E1 4NS, United Kingdom; Email: h.x.yan@qmul.ac.uk

Authors

Zimeng Hu - School of Engineering and Materials Science, Queen Mary University of London, Mile End Road, London E1 4NS, United Kingdom

Gavin B.G. Stenning - ISIS Neutron and Muon Source, Rutherford Appleton Laboratory, Didcot, Oxfordshire OX11 0QX, United Kingdom

Vladimir Koval - Institute of Materials Research, Slovak Academy of Sciences, Kosice 04001, Slovakia

Jiyue Wu - School of Engineering and Materials Science, Queen Mary University of London, Mile End Road, London E1 4NS, United Kingdom

Alisa Leavesley - Thomas Keating Ltd, Billingshurst, West Sussex RH14 9SH, United Kingdom; Virginia Diodes Inc., 979 2nd St SE #309, Charlottesville, VA 22902, USA

Richard Wylde - Thomas Keating Ltd, Billingshurst, West Sussex RH14 9SH, United Kingdom

Michael John Reece - School of Engineering and Materials Science, Queen Mary University of London, Mile End Road, London E1 4NS, United Kingdom

Author Contributions

Zimeng Hu (Carried out laboratory research, data analysis, wrote draft of manuscript), Gavin B.G. Stenning (Conducted the magnetic measurement), Vladimir Koval (Manuscript proofreading), Jiyue Wu (Sample synthesis), Bin Yang (THz measurement), Alisa Leavesley (Magnetizing samples), Richard Wylde (Material design), Michael John Reece (Theoretical discussion), Chenglong Jia (Theoretical discussion) and Haixue Yan (Theoretical discussion and manuscript proofreading).'

Notes

The authors declare no competing financial interest.

REFERENCES

1. Zhai, K.; Shang, D. S.; Chai, Y. S.; Li, G.; Cai, J. W.; Shen, B. G.; Sun, Y., Room-Temperature Nonvolatile Memory Based on a Single-Phase Multiferroic Hexaferrite. *Advanced Functional Materials* **2018,** *28* (9), 1705771.
2. Pullar, R. C., Hexagonal ferrites: A Review of the Synthesis, Properties and Applications of Hexaferrite Ceramics. *Progress in Materials Science* **2012,** *57* (7), 1191-1334.
3. Almessiere, M. A.; Slimani, Y.; Güngüneş, H.; Korkmaz, A. D.; Zubar, T.; Trukhanov, S.; Trukhanov, A.; Manikandan, A.; Alahmari, F.; Baykal, A., Influence of Dy3+ Ions on the Microstructures and Magnetic, Electrical, and Microwave Properties of [Ni0.4Cu0.2Zn0.4](Fe2–xDyx)O4 (0.00 ≤ x ≤ 0.04) Spinel Ferrites. *ACS Omega* **2021,** *6* (15), 10266-10280.
4. Almessiere, M. A.; Slimani, Y.; Trukhanov, A. V.; Baykal, A.; Gungunes, H.; Trukhanova, E. L.; Trukhanov c, S. V.; Kostishin, V. G., Strong Correlation between Dy3+ Concentration, Structure, Magnetic and Microwave Properties of the [Ni0.5Co0.5](DyxFe2-x)O4 Nanosized Ferrites. *Journal of Industrial and Engineering Chemistry* **2020,** *90*, 251-259.
5. Fiebig, M.; Lottermoser, T.; Fröhlich, D.; Goltsev, A. V.; Pisarev, R. V., Observation of Coupled Magnetic and Electric Domains. *Nature* **2002,** *419* (6909), 818-820.
6. Fu, M.; Zhu, Z.; Zhou, Y.; Xu, W.; Chen, W.; Liu, Q.; Zhu, X., Multifunctional Pompon Flower-like Nickel Ferrites as Novel Pseudocapacitive Electrode Materials and Advanced Absorbing Materials. *Ceramics International* **2020,** *46* (1), 850-856.
7. Ashiq, M. N.; Iqbal, M. J.; Gul, I. H., Structural, Magnetic and Dielectric Properties of Zr-Cd Substituted Strontium Hexaferrite (SrFe12O19) Nanoparticles. *Journal of Alloys and Compounds* **2009,** *487* (1-2), 341-345.
8. Ataie, A.; Heshmati-Manesh, S., Synthesis of Ultra-Fine Particles of Strontium Hexaferrite by a Modified Co-precipitation Method. *Journal of the European Ceramic Society* **2001,** *21* (10), 1951-1955.
9. Zi, Z. F.; Sun, Y. P.; Zhu, X. B.; Yang, Z. R.; dai, J. M.; Song, W. H., Structural and Magnetic Properties of SrFe12O19 Hexaferrite Synthesized by a Modified Chemical Co-Precipitation Method. *Journal of Magnetism and Magnetic Materials* **2008,** *320* (21), 2746-2751.
10. Kaur, H.; Marwaha, A.; Singh, C.; Narang, S. B.; Jotania, R.; Jacobo, S.; Sombra, A. S. B.; Trukhanov, S. V.; Trukhanov, A. V.; Dhruv, P., Investigation of Structural, Hysteresis and Electromagnetic Parameters for Microwave Absorption Application in Doped Ba–Sr Hexagonal Ferrites at X-band. *Journal of Alloys and Compounds* **2019,** *806*, 1220-1229.
11. Shen, S.-P.; Chai, Y.-S.; Cong, J.-Z.; Sun, P.-J.; Lu, J.; Yan, L.-Q.; Wang, S.-G.; Sun, Y., Magnetic-Ion-Induced Displacive Electric Polarization in FeO5 Bipyramidal Units of(Ba,Sr)Fe12O19 Hexaferrites. *Physical Review B* **2014,** *90* (18), 180404.
12. Iqbal, M. J.; Ashiq, M. N.; Gul, I. H., Physical, Electrical and Dielectric Properties of Ca-Substituted Strontium Hexaferrite (SrFe12O19) Nanoparticles Synthesized by Co-Precipitation Method. *Journal of Magnetism and Magnetic Materials* **2010,** *322* (13), 1720-1726.

13.   Ullah, Z.; Atiq, S.; Naseem, S., Influence of Pb Doping on Structural, Electrical and Magnetic Properties of Sr-Hexaferrites. *Journal of Alloys and Compounds* **2013,** *555*, 263-267.

14.   Rai, B. K.; Mishra, S. R.; Nguyen, V. V.; Liu, J. P., Synthesis and Characterization of High Coercivity Rare-Earth Ion doped Sr0.9RE0.1Fe10Al2O19 (RE: Y, La, Ce, Pr, Nd, Sm, and Gd). *Journal of Alloys and Compounds* **2013,** *550*, 198-203.

15.   Auwal, I. A.; Güner, S.; Güngüneş, H.; Baykal, A., Sr1-xLaxFe12O19 (0.0≤x≤0.5) Hexaferrites: Synthesis, Characterizations, Hyperfine Interactions and Magneto-Optical Properties. *Ceramics International* **2016,** *42* (11), 12995-13003.

16.   Tang, R.; Zhou, H.; You, W.; Yang, H., Room-temperature Multiferroic and Magnetocapacitance Effects in M-type Hexaferrite BaFe10.2Sc1.8O19. *Applied Physics Letters* **2016,** *109* (8), 082903.

17.   Bsoul, I.; Mahmood, S., Magnetic and Structural Properties of BaFe12− xGaxO19 Nanoparticles. *Journal of Alloys and Compounds* **2010,** *489* (1), 110-114.

18.   Kimura, K.; Ohgaki, M.; Tanaka, K.; Morikawa, H.; Marumo, F., Study of the Bipyramidal Site in Magnetoplumbite-like Compounds, SrM12O19 (M = Al, Fe, Ga). *Journal of Solid State Chemistry* **1990,** *87* (1), 186-194.

19.   Trukhanov, A. V.; Turchenko, V. O.; Bobrikov, I. A.; Trukhanov, S. V.; Kazakevich, I. S.; Balagurov, A. M., Crystal Structure and Magnetic Properties of the BaFe12−xAlxO19 (x=0.1–1.2) Solid Solutions. *Journal of Magnetism and Magnetic Materials* **2015,** *393*, 253-259.

20.   Turchenko, V. A.; Trukhanov, S. V.; Kostishin, V. G.; Damay, F.; Porcher, F.; Klygach, D. S.; Vakhitov, M. G.; Lyakhov, D.; Michels, D.; Bozzo, B.; Fina, I.; Almessiere, M. A.; Slimani, Y.; Baykal, A.; Zhou, D.; Trukhanov, A. V., Features of Structure, Magnetic State and Electrodynamic Performance of SrFe12−xInxO19. *Scientific Reports* **2021,** *11* (1), 18342.

21.   Patel, C. D.; Dhruv, P. N.; Meena, S. S.; Singh, C.; Kavita, S.; Ellouze, M.; Jotania, R. B., Influence of Co4+-Ca2+ Substitution on Structural, Microstructure, Magnetic, Electrical and Impedance Characteristics of M-type Barium–Strontium Hexagonal Ferrites. *Ceramics International* **2020**.

22.   Nguyen, H. H.; Tran, N.; Phan, T. L.; Yang, D. S.; Dang, N. T.; Lee, B. W., Electronic Structure, and Magnetic and Microwave Absorption Properties of Co-doped SrFe12O19 Hexaferrites. *Ceramics International* **2020,** *46* (11), 19506-19513.

23.   Almessiere, M. A.; Slimani, Y.; Tashkandi, N. A.; Baykal, A.; Saraç, M. F.; Trukhanov, A. V.; Ercan, İ.; Belenli, İ.; Ozçelik, B., The Effect of Nb Substitution on Magnetic Properties of BaFe12O19 Nanohexaferrites. *Ceramics International* **2019,** *45* (2, Part A), 1691-1697.

24.   Asghar, G.; Anis-ur-Rehman, M., Structural, Dielectric and Magnetic Properties of Cr-Zn Doped Strontium Hexa-Ferrites for High Frequency Applications. *Journal of Alloys and Compounds* **2012,** *526*, 85-90.

25.   Trukhanov, A. V.; Turchenko, V. A.; Kostishin, V. G.; Damay, F.; Porcher, F.; Lupu, N.; Bozzo, B.; Fina, I.; Polosan, S.; Silibin, M. V.; Salem, M. M.; Tishkevich, D. I.; Trukhanov, S. V., The Origin of the Dual Ferroic Properties in Quasi-Centrosymmetrical SrFe12−xInxO19 Hexaferrites. *Journal of Alloys and Compounds* **2021,** *886*, 161249.

26.   Turchenko, V.; Kostishin, V. G.; Trukhanov, S.; Damay, F.; Balasoiu, M.; Bozzo, B.; Fina, I.; Burkhovetsky, V. V.; Polosan, S.; Zdorovets, M. V.; Kozlovskiy, A. L.; Astapovich, K. A.; Trukhanov, A., Structural Features, Magnetic and Ferroelectric Properties of SrFe10.8In1.2O19 Compound. *Materials Research Bulletin* **2021,** *138*, 111236.

27. Unal, B.; Almessiere, M.; Slimani, Y.; Baykal, A.; Trukhanov, A. V.; Ercan, I., The Conductivity and Dielectric Properties of Neobium Substituted Sr-Hexaferrites. *Nanomaterials* **2019,** *9* (8), 16.

28. Neumann, H.; Arlt, G., Maxwell-Wagner Relaxation and Degradation of SrTiO3 and BaTiO3 Ceramics. *Ferroelectrics* **1986,** *69* (1), 179-186.

29. Yu, C.; Zeng, Y.; Yang, B.; Wylde, R.; Donnan, R.; Wu, J.; Xu, J.; Gao, F.; Abrahams, I.; Reece, M.; Yan, H., SrFe12O19 Based Ceramics with Ultra-low Dielectric Loss in the Millimetre-wave Band. *Applied Physics Letters* **2018,** *112* (14).

30. Ahmed, A.; Prokhorov, A. S.; Anzin, V.; Vinnik, D.; Bush, A.; Gorshunov, B.; Alyabyeva, L., Terahertz-Infrared Electrodynamics of Single-Crystalline Ba0.2Pb0.8Al1.2Fe10.8O19 M-type Hexaferrite. *Journal of Alloys and Compounds* **2020,** *836*.

31. Yang, B.; Donnan, R. S., Enhanced Rapid and Accurate Sub-THz Magneto-Optical Characterization of Hexaferrite Ceramics. *Journal of Magnetism and Magnetic Materials* **2011,** *323* (15), 1992-1997.

32. Almessiere, M. A.; Güner, S.; Slimani, Y.; Hassan, M.; Baykal, A.; Gondal, M. A.; Baig, U.; Trukhanov, S. V.; Trukhanov, A. V., Structural and Magnetic Properties of Co0.5Ni0.5Ga0.01Gd0.01Fe1.98O4/ZnFe2O4 Spinel Ferrite Nanocomposites: Comparative Study between Sol-Gel and Pulsed Laser Ablation in Liquid Approaches. *Nanomaterials* **2021,** *11* (9), 2461.

33. Almessiere, M. A.; Trukhanov, A. V.; Slimani, Y.; You, K. Y.; Trukhanov, S. V.; Trukhanova, E. L.; Esa, F.; Sadaqat, A.; Chaudhary, K.; Zdorovets, M.; Baykal, A., Correlation Between Composition and Electrodynamics Properties in Nanocomposites Based on Hard/Soft Ferrimagnetics with Strong Exchange Coupling. *Nanomaterials* **2019,** *9* (2), 202.

34. Toby, B. H., EXPGUI, a graphical user interface for GSAS. *Journal of applied crystallography* **2001,** *34* (2), 210-213.

35. Larson, A. C.; Von Dreele, R., Program GSAS, General Structure Analysis System. *Los Alamos National Laboratories, Los Alamos* **1994**.

36. Yang, B.; Wang, X.; Zhang, Y.; Donnan, R. S., Experimental characterization of hexaferrite ceramics from 100 GHz to 1 THz using vector network analysis and terahertz-time domain spectroscopy. *Journal of Applied Physics* **2011,** *109* (3), 033509.

37. Jia, L.; Zhang, H.; Zhong, Z.; Liu, Y., Effects of Different Sintering Temperature and Nb2O5 Content on Structural and Magnetic Properties of Z-type Hexaferrites. *Journal of Magnetism and Magnetic Materials* **2007,** *310* (1), 92-97.

38. Glazer, A., ActaCrystallographicaSectionA: CrystalPhysics. *Diffraction, TheoreticalandGeneralCrystallography* **1975,** *31*, 756.

39. Yan, H.; Zhang, H.; Zhang, Z.; Ubic, R.; Reece, M. J., B-site Donor and Acceptor Doped Aurivillius Phase Bi3NbTiO9 Ceramics. *Journal of the European Ceramic Society* **2006,** *26* (13), 2785-2792.

40. Trukhanov, S. V., Investigation of Stability of Ordered Manganites. *Journal of Experimental and Theoretical Physics* **2005,** *101* (3), 513-520.

41. Trukhanov, S. V.; Fedotova, V. V.; Trukhanov, A. V.; Szymczak, H.; Botez, C. E., Cation Ordering and Magnetic Properties of Neodymium-Barium Manganites. *Technical Physics* **2008,** *53* (1), 49-54.

42. Jain, V.; Biesinger, M. C.; Linford, M. R., The Gaussian-Lorentzian Sum, Product, and Convolution (Voigt) Functions in the Context of Peak Fitting X-ray Photoelectron Spectroscopy (XPS) Narrow Scans. *APPLIED SURFACE SCIENCE* **2018,** *447*, 548-553.

43.   Sanjinés, R.; Tang, H.; Berger, H.; Gozzo, F.; Margaritondo, G.; Lévy, F., Electronic Structure of Anatase TiO2 Oxide. *Journal of Applied Physics* **1994,** *75* (6), 2945-2951.

44.   Major, S.; Kumar, S.; Bhatnagar, M.; Chopra, K. L., Effect of Hydrogen Plasma Treatment on Transparent Conducting Oxides. *Applied Physics Letters* **1986,** *49* (7), 394-396.

45.   Szörényi, T.; Laude, L. D.; Bertóti, I.; Kántor, Z.; Geretovszky, Z., Excimer Laser Processing of Indium-Tin-Oxide Films: An Optical Investigation. *Journal of Applied Physics* **1995,** *78* (10), 6211-6219.

46.   Zhang, B.; Wang, J.; Zou, T.; Zhang, S.; Yaer, X.; Ding, N.; Liu, C.; Miao, L.; Li, Y.; Wu, Y., High Thermoelectric Performance of Nb-Doped SrTiO3 Bulk Materials with Different Doping Levels. *Journal of Materials Chemistry C* **2015,** *3* (43), 11406-11411.

47.   Oku, M.; Hirokawa, K., X-ray Photoelectron Spectroscopy of Co3O4, Fe3O4, Mn3O4, and Related Compounds. *Journal of Electron Spectroscopy and Related Phenomena* **1976,** *8* (5), 475-481.

48.   Zhong, Y.; Yu, L.; Chen, Z.-F.; He, H.; Ye, F.; Cheng, G.; Zhang, Q., Microwave-Assisted Synthesis of Fe3O4 Nanocrystals with Predominantly Exposed Facets and Their Heterogeneous UVA/Fenton Catalytic Activity. *ACS Applied Materials & Interfaces* **2017,** *9* (34), 29203-29212.

49.   Trukhanov, S. V.; Bushinsky, M. V.; Troyanchuk, I. O.; Szymczak, H., Magnetic Ordering in La1−xSrxMnO3−x/2 Anion-Deficient Manganites. *Journal of Experimental and Theoretical Physics* **2004,** *99* (4), 756-765.

50.   Yang, Y.; Wang, F.; Shao, J.; Huang, D.; Trukhanov, A. V.; Trukhanov, S. V., Structural, Spectral, Magnetic, and Electrical Properties of Gd–Co-co-Substituted M-type Ca–Sr Hexaferrites Synthesized by the Ceramic Method. *Applied Physics A* **2018,** *125* (1), 37.

51.   Shirk, B. T.; Buessem, W. R., Temperature Dependence of Ms and K1 of BaFe12O19 and SrFe12O19 Single Crystals. *Journal of Applied Physics* **1969,** *40* (3), 1294-1296.

52.   Li, Z.; Koval, V.; Mahajan, A.; Gao, Z.; Vecchini, C.; Stewart, M.; Cain, M. G.; Tao, K.; Jia, C.; Viola, G.; Yan, H., Room-temperature Multiferroic Behavior in Layer-structured Aurivillius Phase Ceramics. *Applied Physics Letters* **2020,** *117* (5), 052903.

53.   Zhang, M.; Chen, Z.; Yue, Y.; Chen, T.; Yan, Z.; Jiang, Q.; Yang, B.; Eriksson, M.; Tang, J.; Zhang, D., Terahertz Reading of Ferroelectric Domain Wall Dielectric Switching. *ACS Applied Materials & Interfaces* **2021,** *13* (10), 12622-12628.

54.   Yan, H.; Reece, M. J.; Liu, J.; Shen, Z.; Kan, Y.; Wang, P., Effect of Texture on Dielectric Properties and Thermal Depoling of Bi4Ti3O12 Ferroelectric Ceramics. *Journal of Applied Physics* **2006,** *100* (7), 076103.

55.   Shulman, H. S.; Damjanovic, D.; Setter, N., Niobium Doping and Dielectric Anomalies in Bismuth Titanate. *Journal of the American Ceramic Society* **2000,** *83* (3), 528-532.

56.   Härdtl, K., Electrical and Mechanical Losses in Ferroelectric Ceramics. *Ceramics International* **1982,** *8* (4), 121-127.

57.   Fang, Q.; Bao, H.; Fang, D.; Wang, J., Temperature Dependence of Magnetic Properties of Zinc and Niobium Doped Strontium Hexaferrite Nanoparticles. *Journal of Applied Physics* **2004,** *95* (11), 6360-6363.

58.   Troyanchuk, I. O.; Trukhanov, S. V.; Shapovalova, E. F.; Khomchenko, V. A.; Tovar, M.; Szymczak, H., The Influence of Oxygen Vacancies on the Magnetic State of La0.50D0.50MnO3−γ (D=Da, Sr) Manganites. *Journal of Experimental and Theoretical Physics* **2003,** *96* (6), 1055-1064.

59.   Humbe, A. V.; Kounsalye, J. S.; Shisode, M. V.; Jadhav, K., Rietveld Refinement, Morphology and Superparamagnetism of Nanocrystalline Ni0.70-xCuxZn0.30Fe2O4 Spinel Ferrite. *Ceramics International* **2018,** *44* (5), 5466-5472.

60.   Dai, J. F.; Wen, X. C.; Feng, W.; Cheng, C.; Huang, D. Q., Correlation of the Heat Treatment Feature and Magnetic Properties of the SrFe12O19@ZnFe2O4 Core-Shell Nanofibers. *MATERIALS CHEMISTRY AND PHYSICS* **2022,** *276*, 125393.

61.   Ashiq, M. N.; Qureshi, R. B.; Malana, M. A.; Ehsan, M. F., Fabrication, Structural, Dielectric and Magnetic Properties of Tantalum and Potassium Doped M-type Strontium Calcium Hexaferrites. *Journal of Alloys and Compounds* **2015,** *651*, 266-272.

62.   Trukhanov, S. V.; Zubar, T. I.; Turchenko, V. A.; Trukhanov, A. V.; Kmječ, T.; Kohout, J.; Matzui, L.; Yakovenko, O.; Vinnik, D. A.; Starikov, A. Y.; Zhivulin, V. E.; Sombra, A. S. B.; Zhou, D.; Jotania, R. B.; Singh, C.; Trukhanov, A. V., Exploration of Crystal Structure, Magnetic and Dielectric Properties of Titanium-barium Hexaferrites. *Materials Science and Engineering: B* **2021,** *272*, 115345.

63.   Turchenko, V. A.; Trukhanov, S. V.; Kostishin, V. G. e.; Damay, F.; Porcher, F.; Klygach, D. S.; Vakhitov, M. G. e.; Matzui, L. Y. e.; Yakovenko, O. S.; Bozzo, B.; Fina, I.; Almessiere, M. A.; Slimani, Y.; Baykal, A.; Zhou, D.; Trukhanov, A. V., Impact of In3+ Cations on Structure and Electromagnetic State of M−type Hexaferrites. *Journal of Energy Chemistry* **2022,** *69*, 667-676.

64.   Trukhanov, S. V., Peculiarities of the Magnetic State in the System La0.70Sr0.30MnO3−γ (0 ≤ γ ≤ 0.25). *Journal of Experimental and Theoretical Physics* **2005,** *100* (1), 95-105.

65.   Trukhanov, S. V.; Trukhanov, A. V.; Vasiliev, A. N.; Balagurov, A. M.; Szymczak, H., Magnetic State of the Structural Separated Anion-Deficient La0.70Sr0.30MnO2.85 Manganite. *Journal of Experimental and Theoretical Physics* **2011,** *113* (5), 819-825.

66.   Sudakar, C.; Subbanna, G. N.; Kutty, T. R. N., Wet Chemical Synthesis of Multicomponent Hexaferrites by Gel-to-Crystallite Conversion and Their Magnetic Properties. *Journal of Magnetism and Magnetic Materials* **2003,** *263* (3), 253-268.

67.   Coey, J. M., *Magnetism and Magnetic Materials*. Cambridge university press: 2010.

68.   Herzer, G., Grain Size Dependence of Coercivity and Permeability in Nanocrystalline Ferromagnets. *IEEE Transactions on magnetics* **1990,** *26* (5), 1397-1402.

69.   Guzmán-Mínguez, J. C.; Moreno-Arche, L.; Granados-Miralles, C.; López-Sánchez, J.; Marín, P.; Fernández, J. F.; Quesada, A., Boosting the Coercivity of SrFe12O19 Nanocrystalline Powders Obtained Using the Citrate Combustion Synthesis Method. *Journal of Physics D: Applied Physics* **2020,** *54* (1), 014002.

70.   de Julian Fernandez, C.; Sangregorio, C.; de la Figuera, J.; Belec, B.; Makovec, D.; Quesada, A., Topical Review: Progress and Prospects of Hard Hexaferrites for Permanent Magnet Applications. *Journal of Physics D: Applied Physics* **2020**, 153001.

71.   Yadav, A. K.; Anita, A.; Kumar, S.; Panchwanee, A.; Reddy, V. R.; Shirage, P. M.; Biring, S.; Sen, S., Structural and Ferroelectric Properties of Perovskite Pb(1−x)(K0.5Sm0.5)xTiO3 Ceramics. *RSC Advances* **2017,** *7* (63), 39434-39442.

Table of Contents

Linearly Polarized THz signal

Faraday Rotation

Magnets